

# Precise Relocation and Source Characterization of Two Earthquake Sequences in Yellow Sea Using Regional *Lg*-Wave Observations

Jun Yong Park<sup>1</sup> , Won-Young Kim<sup>2</sup> , YoungHee Kim<sup>\*1</sup> , and Xuzhang Shen<sup>3</sup>

## ABSTRACT

Two significant earthquakes of magnitude  $M_L$  4.6 and 4.5 occurred on 18 January and 3 December 2021 in the central region of the Yellow Sea, respectively. The earthquakes occurred beneath the Gunsan sedimentary basin at about 10 km depth with a strike-slip faulting mechanism on nodal planes striking northwest–southeast (NW–SE) and north-northeast–south-southwest (NNE–SSW). Despite a lack of close-by seismographic stations, we successfully utilized regional *Lg*-wave observations on both coasts of the sea—the Korean peninsula on the east and eastern China on the west. For nine earthquakes in two event sequences, the *Lg*-wave differential travel times of the nearby event pairs at the common station are carefully measured using the waveform cross-correlation technique. The double-difference earthquake relocation method is employed to obtain precise relative epicentral locations using the *Lg* correlation measurements. Relocated epicenters align along the NW–SE direction, indicating that the nodal plane striking the same direction is the likely fault plane on which both sequences occurred. This is the first case reported in the literature in which the causative fault plane has been identified for earthquakes in the central Yellow Sea region. It has an important implication for current regional tectonics; it favors neither old tectonic features trending NE–SW (Qianliyan uplift) nor the north–south alignment of significant earthquakes in the region along the Amur plate boundary. The *Lg* waves from the earthquake sequences are dominant seismic signals on all three-component records at stations in 160–550 km and allowed us to analyze source properties of the two largest earthquakes using the empirical Green's function approach. Azimuthal variations of the source corner frequencies suggest that earthquake rupture likely propagated toward southeast (125°) along the fault plane, supporting the aftershock relocation results.

## KEY POINTS

- We analyzed two earthquake sequences that occurred in the central region of the Yellow Sea using regional *Lg* waves.
- Relocated earthquakes using *Lg*-wave cross-correlation measurements align along the northwest–southeast (NW–SE) direction.
- Azimuthal variations of corner frequencies suggest rupture toward SE, supporting the aftershock locations.

## Supplemental Material

keen interest among seismologists in Korea because the sequence occurred in the Gunsan basin, the eastern part of the northern South Yellow Sea basin (NSYSB), where no known earthquakes of magnitude greater than four have occurred since 1978 (Fig. 1a). Most earthquakes in the central Yellow Sea region have occurred off the three major sedimentary basins (Fig. 1a) (e.g., Choi *et al.*, 2015). On 3 December

1. School of Earth and Environmental Sciences, Seoul National University, Seoul, Republic of Korea,  <https://orcid.org/0000-0003-2244-0210> (JYP);  <https://orcid.org/0000-0002-1111-632X> (YHK); 2. Lamont-Doherty Earth Observatory of Columbia University, Palisades, New York, U.S.A.,  <https://orcid.org/0000-0002-0005-9681> (W-YK); 3. Guangdong Provincial Key Lab of Geodynamics and Geohazards, School of Earth Sciences and Engineering, Sun Yat-Sen University, Guangzhou, China

\*Corresponding author: youngkim@snu.ac.kr

Cite this article as Park, J. Y., W.-Y. Kim, Y.H. Kim, and X. Shen (2024). Precise Relocation and Source Characterization of Two Earthquake Sequences in Yellow Sea Using Regional *Lg*-Wave Observations, *Bull. Seismol. Soc. Am.* **XX**, 1–17, doi: [10.1785/0120240067](https://doi.org/10.1785/0120240067)

© Seismological Society of America

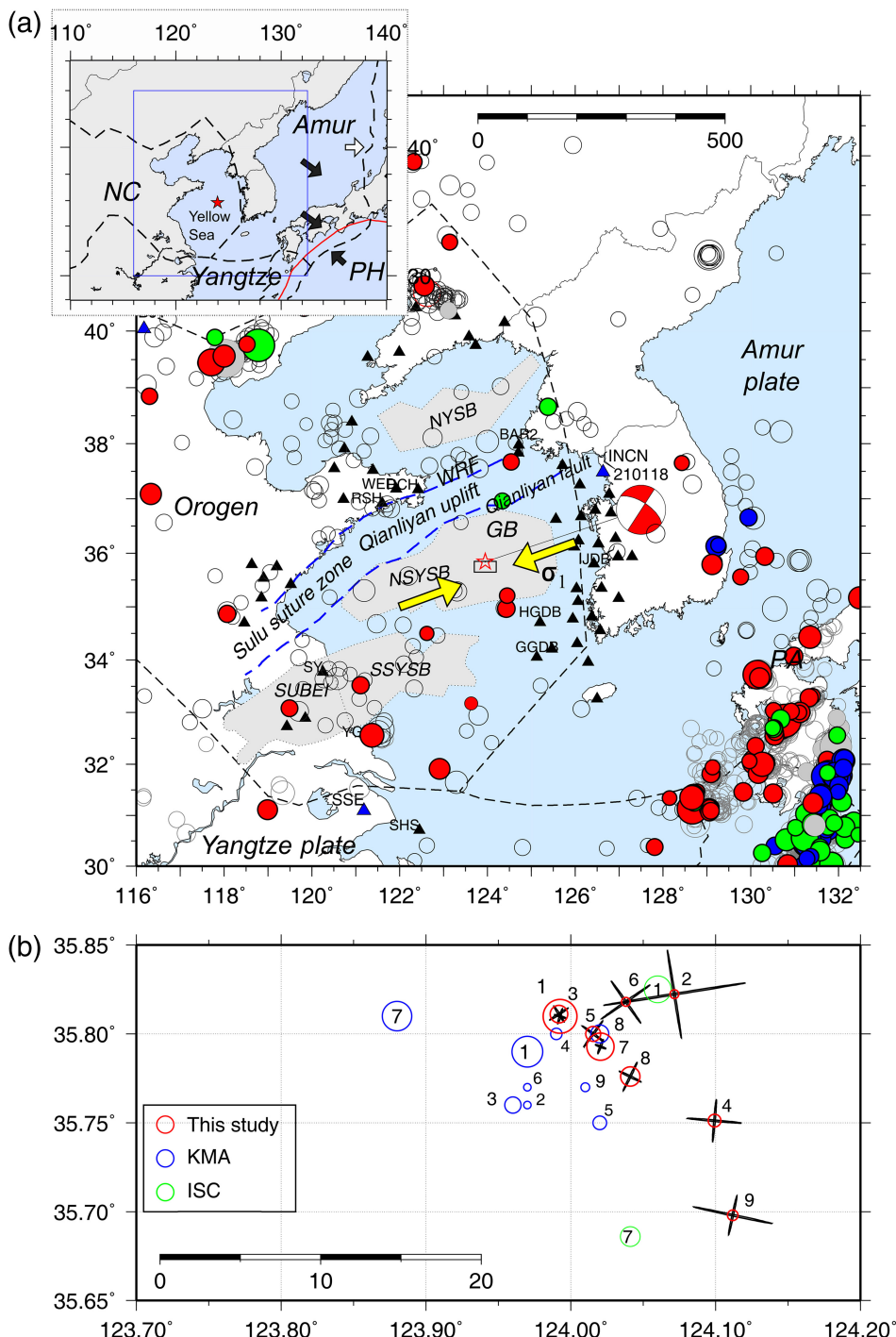


**Figure 1.** (a) Earthquakes during 1976–2023 from the Global Centroid Moment Tensor (Global CMT) catalog are plotted by filled circles, and focal mechanisms are color-coded: strike-slip (red), normal faulting (green), and thrust (blue). The mainshock of the 2021 Offshore Gunsan earthquake is denoted by a red star in the inset figure, and its focal mechanism is shown as a focal mechanism plot with a lower hemispheric projection. The location of our study area is marked as a black rectangle. Earthquakes of magnitude  $m_b > 4.0$  during 1978–2020 from the International Seismological Centre (ISC) catalog are plotted by open circles to show background seismicity. Used seismographic stations around the Yellow Sea are plotted by filled triangles. All the stations are plotted in Figure S1a. Sedimentary basins in the Yellow Sea are represented as gray shaded areas: GB, Gunsan basin; NYSB, northern south Yellow Sea basin; NYSB, north Yellow Sea basin; and SSYSB, southern south Yellow Sea basin. Triassic–Jurassic collision zone between the northern Sino-Korean and southern Yangtze blocks is represented as a broad suture zone along the Wulian–Rongcheng fault (WRF) and Sulu suture–Qianliyan fault. The trend of the compressional stress axis  $\sigma_1$  is drawn with yellow arrows. (b) Earthquakes of the 2021 Offshore Gunsan earthquake sequences reported by the Korea Meteorological Administration (KMA) (blue circles), ISC (green circles), and nine events located in this study (red circles). Location uncertainties in horizontal and vertical directions in 95% confidence level are indicated by error bars on those events located in this study. For smaller events 3, 4, 5, and 8, their ISC epicenters are outside the map range. The color version of this figure is available only in the electronic edition.

northern south Yellow Sea basin; NYSB, north Yellow Sea basin; and SSYSB, southern south Yellow Sea basin. Triassic–Jurassic collision zone between the northern Sino-Korean and southern Yangtze blocks is represented as a broad suture zone along the Wulian–Rongcheng fault (WRF) and Sulu suture–Qianliyan fault. The trend of the compressional stress axis  $\sigma_1$  is drawn with yellow arrows. (b) Earthquakes of the 2021 Offshore Gunsan earthquake sequences reported by the Korea Meteorological Administration (KMA) (blue circles), ISC (green circles), and nine events located in this study (red circles). Location uncertainties in horizontal and vertical directions in 95% confidence level are indicated by error bars on those events located in this study. For smaller events 3, 4, 5, and 8, their ISC epicenters are outside the map range. The color version of this figure is available only in the electronic edition.

TABLE 1  
Events of the 2021 Gunsan Basin, Yellow Sea Earthquake Sequences

ID	Date (yyyy/mm/dd)	Time (UTC) (hh:mm:ss.ss)	Latitude (°N)	Longitude (°E)	Depth (km)	Magnitude			
						$M_L^t$	$M_w^f$	$H_{err}$ (km) <sup>s</sup>	Gap (°)
1	2021/01/18	18:21:28.17	35.8099	123.9926	10*	4.6	4.7	1.0	43
2	2021/01/19	13:58:32.28	35.8223	124.0715	10	1.9	—	9.0	146
3	2021/01/21	21:01:49.24	35.8112	123.9918	10	3.2	—	1.5	97
4	2021/01/29	13:34:55.54	35.7512	124.0992	10	2.6	—	3.4	173
5	2021/02/04	01:56:19.66	35.8000	124.0155	10	2.9	3.5	2.3	98
6	2021/03/09	17:56:25.10	35.8180	124.0380	10	1.9	—	4.1	157
7	2021/12/03	12:08:22.86	35.7928	124.0205	10*	4.5	4.2	1.0	64
8	2021/12/03	15:18:10.25	35.7760	124.0410	10	3.4	3.5	2.1	98
9	2021/12/04	00:30:18.78	35.6980	124.1118	10	2.2	—	5.0	281

Date, time, latitude, longitude, depth, and  $H_{err}$  are from HYPOINVERSE event location.

\*Depth is from the waveform modeling (events 1 and 7).

<sup>t</sup> $M_L$  is the local magnitude reported by the Korea Meteorological Administration (KMA).

<sup>f</sup> $M_w$  is the moment magnitude derived from the seismic moment from waveform inversion for events 1 and 7;  $M_w$  from the moment ratio from spectral analysis for events 5 and 8.

<sup>s</sup> $H_{err}$  is the crude horizontal location uncertainty at a 95% confidence level.

2021, after 11 months of quiescence in the epicentral area, an  $M_L$  4.5 earthquake occurred about 8 km west of the January earthquake. Two small aftershocks of  $M_L$  2.2 and 3.4 followed the December earthquake within 12 hr, and then seismicity in the area became quiet (Table 1).

The Yellow Sea is a vast shallow water basin (less than 100 m depth) enclosed by the Korean peninsula in the east, the Bohai Sea in the north, and the Shandong peninsula and eastern China in the west; it continues to the east China Sea in the south below 33° N (Fig. 1a). Sediments mostly cover the seafloor, but its bedrock consists of Archean–Proterozoic rocks of the Korean peninsula and Paleozoic and younger formations on eastern China sides of the sea. The epicentral region is close to the Triassic collision zone between the north and south China blocks proposed in several tectonic models, which runs abutting the northern boundary of the NSYSB along the Qianliyan uplift (Fig. 1a; Choi *et al.*, 2015).

Since the 1990s, reported medium-sized earthquakes ( $M \sim 4.5\text{--}5.0$ ), including the 2021 earthquake sequences, have occurred along north–south (N–S) parallel to the Amur plate boundary (Bird, 2003) to the west (Fig. 1a). Earthquakes in the Yellow Sea with known focal mechanisms are mostly strike-slip faulting mechanisms, with normal-faulting earthquakes located along the Triassic–Jurassic collision zone north of the 2021 earthquake sequences and south of the NYSB (e.g., Yin and Nie, 1993; Chough *et al.*, 2006; Hong and Choi, 2012). The P- and T-axis orientations of those known focal mechanisms indicate that  $\sigma_1$  axis trends east-northeast–west-southwest (ENE–WSW) and plunges 20°. The trend of the stress axes is consistent with a regional horizontal compression in and around the Korean peninsula (Soh *et al.*, 2018), but the plunge angle is about 15° greater than the regional subhorizontal compressional stress, suggesting a transtensional tectonic stress regime that allowed normal-faulting earthquakes. Hence, the

strike-slip faulting mechanism for the 2021 Gunsan earthquake sequences may be expected.

Previously, Rhee and Kim (2010) reported focal mechanisms of a dozen earthquakes that occurred in 2001–2008; Park *et al.* (2012) analyzed the  $M_L$  5.3 earthquake on 12 January 2011 in southern Yellow Sea; Son *et al.* (2015) reported  $M_w$  4.9 earthquake on 17 May 2013 and  $M_L$  3.8 earthquake on 3 June 2013; Hu *et al.* (2022) analyzed  $M_w$  5.0 earthquake on 17 November 2021, at Yancheng City, SSYSB. The majority of the focal mechanisms reported are strike-slip faulting on near-vertical nodal planes with a few normal-faulting events with east-west-trending nodal planes. In most of these studies, authors constrained focal mechanisms of moderate-size events ( $M > 4.5$ ) but were unable to identify the actual fault plane among the two nodal planes: north-northeast–northeast (NNE–NE, ~30°)-trending right-lateral strike-slip faulting and the west-northwest–northwest (WNW–NW, ~300°)-trending left-lateral strike-slip faulting. This is obviously due to the lack of close-in seismographic stations because the epicentral areas are in offshore oceanic environments. Hence, even if small aftershocks accompany those main earthquakes, those small aftershocks could not be located confidently to assist in identifying any lineament related to the earthquake faulting. It is crucial to identify the fault plane in each of those large events because fault motions may guide us to determine whether the fault striking NE might be related to the N–S-trending plate boundary of the Amur plate (see Fig. 1a) or motions related to the NW trend that may suggest active seismogenic fault motion across the Yellow Sea in the E–W direction.

Absolute earthquake locations are traditionally obtained using arrival-time picks of  $P$  and  $S$  waves and location programs such as HYPOINVERSE (Klein, 2002). At local and regional distances—a few tens to hundreds of kilometers from the source,  $P$  and  $S$  direct waves, as well as  $Pn$  and  $Sn$  refracted

phases, are mostly utilized to locate seismic events. However, for earthquakes in the Yellow Sea, because the nearest stations were at least 160 km away from the sources, the conventional method that uses  $Pn$  and  $Sn$  arrival times is not effective in locating the events, especially small earthquakes (usually  $M < 3.0$ ) with weak signal amplitudes, which make it hard to pick clear phase arrival times.

In recent years, the  $Lg$  wave has been effectively utilized in seismic event locations because  $Lg$  waves are the largest amplitude signals on regional seismic records.  $Lg$  waves are well developed at stations beyond  $\sim 150$  km (about five times the crustal thickness) along continental paths through the stable crust (e.g., Knopoff *et al.*, 1973; Kennett, 1986). The key to the successful use of the  $Lg$  wavetrain is the waveform similarity from seismic events located close together observed at a common station. Hence, the  $Lg$  waveform cross-correlation (WCC) technique can detect and locate repeating events using the master event with a known location (e.g., Schaff and Richards, 2004a,b). The  $Lg$  WCC is also used to measure precise differential travel times ( $dt$ ) of event pairs in a double-difference (DD) earthquake relocation scheme to relocate clusters of seismic events with great success (Schaff, Kim, *et al.*, 2018; Schaff, Richards, *et al.*, 2018). Here, we utilize the  $Lg$  WCC technique to measure high-precision  $dt$  of event pairs and relocate two earthquake sequences in the Gunsan basin. We closely follow the method of Schaff, Richards, *et al.* (2018) to locate the earthquake clusters for epicentral coordinates and centroid time in the DD algorithm with a fixed depth.

In this study, we compiled waveform data from over 150 stations in eastern China and the southern Korean peninsula, unprecedented for an earthquake study in the Yellow Sea. The main objective of this article is (1) to identify the seismogenic fault of the 2021 Gunsan basin earthquake sequences by employing the DD earthquake relocation method based on  $Lg$ -wave correlation measurements, (2) to understand the spatiotemporal behavior of the 2021 earthquake sequences with 11 months of delay between the two sequences, and (3) to reveal details about the rupture process of the two large target main events by employing the empirical Green's function (EGF) approach.

## REGIONAL SEISMIC OBSERVATION AND FOCAL MECHANISM AND DEPTH DETERMINATION

The 2021 Gunsan basin earthquakes occurred in the central region of the Yellow Sea, at least 160 km from the nearest seismographic stations on land in the southern Korean peninsula and eastern China (Fig. 1a, Fig. S1, available in the supplemental material to this article). At this regional distance range, the  $Pn$  phase is the first arrival at all seismographic stations around the epicenter, followed by other regional phases such as  $Pg$ ,  $Sn$ , and  $Sg$ , as shown in Figure 2. The first-arrival  $Pn$  phases are weak at all stations, and the  $Sn$  phase is rarely identifiable on most records (Fig. 2). Although the  $Pn$  phase is recognized on

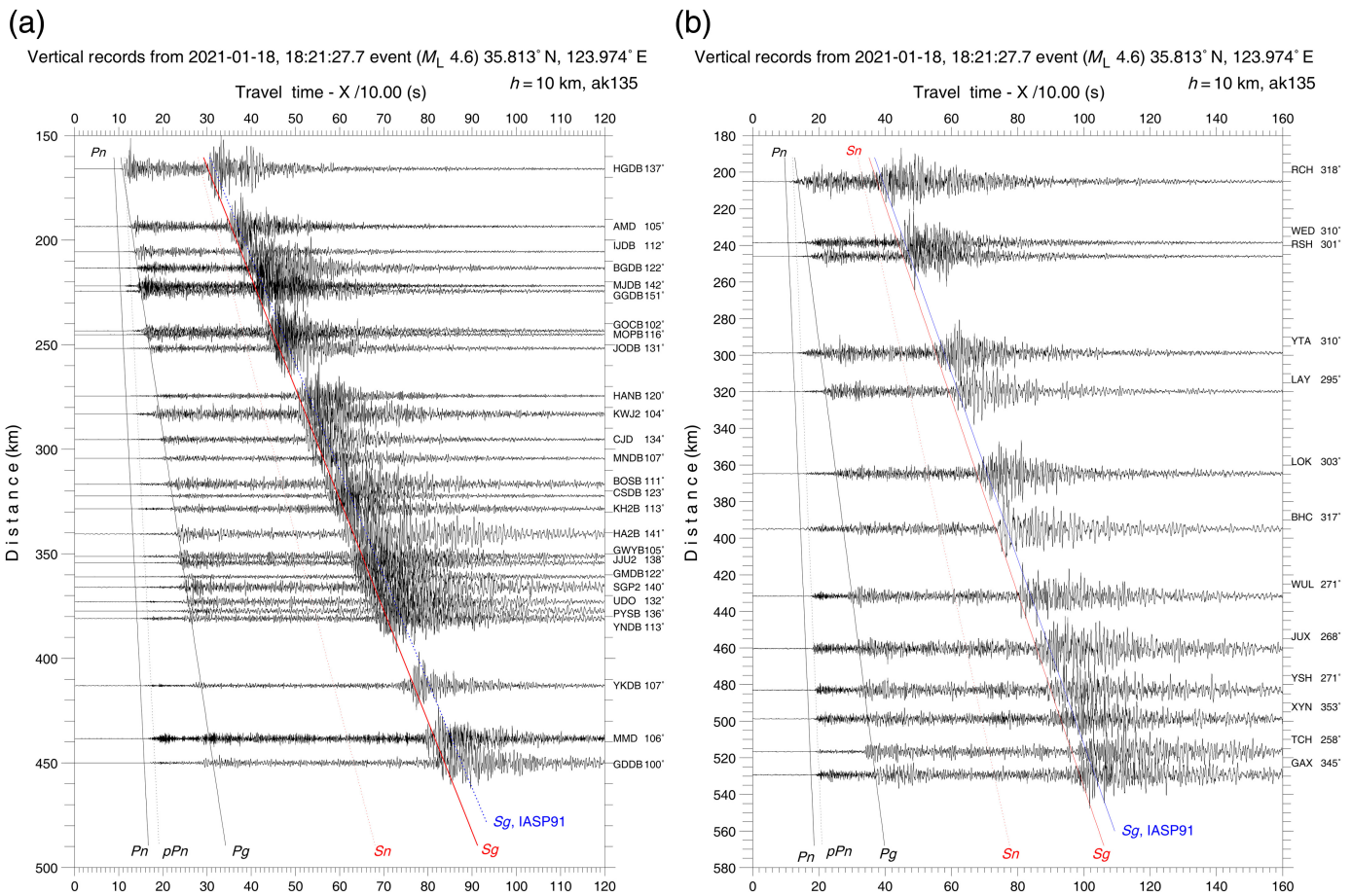
records from the  $M_L$  4.6 event, which arrives with a group velocity range from 6.4 to 7.4 km/s, it is difficult to pick  $Pn$  arrivals with certainty on records from smaller events due to the small amplitude of the  $Pn$  phases and high level of ambient noise. The  $Sn$  phase is even harder to identify and pick arrivals with confidence at most stations due to noise and the preceding  $P$ -wave coda.

$Pg$  and  $Sg$  waves are strong, and their arrivals are consistent over a wide distance range, suggesting that the gross crustal structure underneath the Yellow Sea is a typical continental crust with no obvious disturbances along various paths (Fig. 2). Hong and Choi (2012) analyzed seismograms from two earthquakes in eastern China (18 June 2006  $M_L$  3.6 and 4 July 2006  $M_w$  4.9) recorded at stations in the Korean peninsula. They reported that major regional phases ( $Pn$ ,  $Pg$ ,  $Sn$ ,  $Lg$ , and  $Rg$ ) are well observed at all stations and suggested the minimal lateral variation in the continental crust beneath the Yellow Sea. It is noted that the  $Sg$  arrivals usually mark the beginning of the  $Lg$  wavetrain, as shown in Figure 2 (Kim, 1987). The observed  $Sg$  arrivals from the earthquake show an apparent speed of 3.57 km/s over the distance range from 160 to 450 km, as shown in Figure 2, and align consistently slightly faster than the travel times predicted by the ak135 velocity model (Kennett *et al.*, 1995), which has a crustal average velocity of  $V_S = 3.63$  km/s (see Fig. S2a). This is also faster than the travel times of the  $Sg$  phase calculated by the IASP91 model (Kennett and Engdahl, 1991), which has an average crustal velocity of  $V_S = 3.53$  km/s (see Fig. S2a).

## Focal mechanism and depth of the 18 January and 3 December 2021 earthquakes

For earthquakes in the middle of the Yellow Sea, it is nearly impossible to determine a reliable focal mechanism using the  $P$ -wave first-motion polarities due to the lack of local  $P$  and  $S$  arrivals with diverse takeoff angles leaving the source. We determined the focal mechanisms of the two mainshocks of the 2021 Gunsan basin earthquake sequence and constrained focal depths by modeling observed long-period waveforms and inverted for the deviatoric moment tensor (double-couple source). We selected waveform data from 47 broadband stations in the epicentral distance range from 160 km (HGDB) to 1538 km (HIA) with wide azimuthal coverage in the Korean peninsula, Japan, and China (Fig. S3). In addition to stations of the national networks in Korea, Japan, and China, the Global Seismic Network (GSN) stations INCN (294 km, AZ = 50°), BJT (838 km, AZ = 306°), MDJ (1085 km, AZ = 24°), and HIA (1538 km, AZ = 348°) provided additional coverage (Fig. S3). The observed long-period body waves,  $Pnl$  and  $Snl$ , as well as fundamental-mode surface waves are the main signals for the source mechanism inversion.

Two 1D crustal velocity models are used to calculate regional synthetics. The base model is a two-layer crustal model given by Kim and Kim (1983), and the second model



is constructed by replacing the top 2 km with a low-velocity surface layer ( $V_p = 3.0$  km/s; Kim *et al.*, 2022). The model with the low-velocity surface layer is used for wave propagation paths to stations in eastern China (Jiangsu and Shandong provinces; see Figs. S3 and S4). We modeled the complete waveform, including body and surface waves, in the period between 10 and 33 s for regional records (Fig. S4). We followed the approach described by Kim *et al.* (2010) to model three-component displacement records using the frequency–wave-number integration method for a point source embedded in a 1D crustal velocity model.

We inverted the focal mechanism parameters as a grid search through the whole parameter space of strike, dip, rake, and seismic moment ( $M_0$ ) (Zhao and Helmberger, 1994; Kim *et al.*, 2010). The method matches observed seismograms against synthetics over whole wavetrains and allows relative time shifts between observed and synthetic traces (Fig. S4; Zhao and Helmberger, 1994). We obtained a predominantly strike-slip-faulting mechanism along steeply dipping (65° and 77°) nodal planes striking 207° and 303° and horizontal  $P$ -axis trending WSW (257°) (Fig. S4, Table 2). The  $P$ -axis orientation is consistent with other known shallow earthquakes in the region (Kim *et al.*, 2006; Park *et al.*, 2007).

The long-period body waves are sensitive to source depth because of changes in relative amplitudes of initially upgoing

**Figure 2.** (a) Vertical record section of regional seismograms from the  $M_L$  4.6 earthquake on 18 January 2021 that occurred in the Gunsan basin in the Yellow Sea. Selected stations in the Korean peninsula situated along the azimuth range 100°–151° and distance range from 165 to 450 km are plotted with a reduced velocity of 10 km/s. Travel times of regional phases calculated with the ak135 crustal model (Kennett *et al.*, 1995) are indicated by black and red lines. Notice the weak first-arrival  $Pn$  phases followed by the visible  $pPn$  phase that started as an upgoing  $P$  wave at the source and reflected at the surface (or at the seafloor), and  $Sn$  is not discernible. Crustal phases,  $Pg$  and  $Sg$  ( $Lg$ ), dominate the regional records. The red line denotes travel times calculated using the ak135 model, whereas the dotted line is travel times for the IASP91 model (Kennett and Engdahl, 1991). (b) Vertical record section of regional seismograms from the  $M_L$  4.6 earthquake on 18 January 2021 that occurred in the Gunsan basin in the Yellow Sea. Selected stations in eastern China situated along the azimuth range 258°–353° and distance range from 205 to 540 km are plotted with a reduced velocity of 10 km/s. Travel times of regional phases calculated with the ak135 crustal model are indicated by black and red lines. Notice the weak first-arrival  $Pn$  phases followed by the visible  $pPn$  phase (dotted line) that started as an upgoing  $P$  wave at the source and reflected at the surface (or at the seafloor), and  $Sn$  is not discernible. Crustal phases,  $Pg$  and  $Sg$  ( $Lg$ ) dominate the regional records as in the stations in the Korean peninsula (Fig. 2a). The color version of this figure is available only in the electronic edition.

and downgoing waves at the source and, hence, are very useful to constrain source depth. The focal depth for the two main-shocks is obtained by running the waveform inversion for a

TABLE 2

**Seismic Moment and Focal Mechanism of Two Largest Events from Waveform Moment Tensor Inversion**

ID	$M_w$	Seismic Moment ( $10^{16}$ N·m)	Depth (km)*	NP1 <sup>†</sup>	NP2	P Axis
				s (°)/d (°)/r (°)	s (°)/d (°)/r (°)	tr (°) /pl (°)
1	4.71	1.29 ( $\pm 1.08$ )	10.0	303/65/14	207/77/154	257/8
7	4.23	0.24 ( $\pm 0.17$ )	10.0	307/70/18	211/73/159	259/2

d, dip; pl, plunge; r, rake; s, strike; and tr, trend.

\*Depth is determined from the waveform modeling for mechanism inversion.

<sup>†</sup>NP1 and NP2 are two nodal planes of the best-fitting double-couple solution of the focal mechanism.

range of focal depths with a 1 km interval and seeking the global minimum of the misfit as shown in Figure S5. The waveform inversions constrained focal depth of  $10 \pm 2$  km with the fitting error minimum (Fig. S5).

## EVENT LOCATION AND RELOCATION USING $Pn$ AND $Sn$ ARRIVAL-TIME PICKS

### Single event locations

On 18 January 2021, the KMA reported an  $M_L$  4.6 earthquake (event 1) followed by five smaller aftershocks. In addition, on 3 December 2021, the KMA reported an  $M_L$  4.5 earthquake (event 7) accompanied by two minor aftershocks (Fig. 1b). The location accuracy of these earthquakes may be very low due to the lack of nearby local seismographic stations around the epicenter. The International Seismological Centre (ISC) bulletin reports six out of the nine events in the two earthquake sequences, as listed in Table S1. For Event 1, the ISC location is about 9 km ENE from the KMA location, whereas for Event 7, the ISC location is 20 km SE from the KMA location, as shown in Figure 1b.

The  $Pn$  phase is the crucial regional phase for the location of earthquakes in the Yellow Sea by a conventional location method utilizing the first arrival body-wave phases.  $Pn$  arrivals are weak but clear at most stations in distances from 160 to 550 km, as shown in Figure 2 (see also Fig. S2b,c). Although the amplitudes of  $Pn$  phase arrivals are quite small, the observed arrival times align well along the calculated  $Pn$  travel-time curve from an average global continental crustal velocity model, ak135 (Kennett *et al.*, 1995) (Fig. S2).  $Sn$  phase arrivals are not readily discernable on seismic records from the Korean peninsula and China (Fig. 2).

We manually picked arrival times of the  $Pn$  phase at 33 selected stations in eastern China in the distance range 207–585 km and covering azimuth from  $195^\circ$  to  $7^\circ$  with at least a station in each  $5^\circ$  azimuth interval. We selected 34 stations in the Korean peninsula in the distance range of 164–364 km with azimuth coverage from  $14^\circ$  to  $141^\circ$  (Fig. 1a, Fig. S1).  $Sn$  phases are also picked at about one-third of the stations for events greater than magnitude three, in which we can identify their arrivals. We located events using a location program HYPOINVERSE (Klein, 2002) with a two-layer crustal velocity

model (Kim and Kim, 1983). We located the nine events with a fixed depth of 10 km as constrained by the long-period waveform modeling (Figs. S5) because we used  $Pn$  arrivals exclusively to locate, and hence, focal depth could not be well constrained by arrival-time pick data.

Epicenter locations of the nine earthquakes of the 2021 earthquake sequences are plotted in Figure 1b and are listed in Table 1. Five larger events with magnitude  $M_L \geq 2.9$  are located with the root mean square (rms) residual less than 0.5 s and are clustered closely along the strike direction of the nodal plane 1 (Fig. 1b; NP1 in Table 2). Hence, their locations are considered satisfactory, given the lack of nearby stations. The absolute locations of the largest two events, events 1 and 7, lie about 3 km NE and 13 km east of the KMA locations, respectively (Fig. 1b). The three smallest events with  $M_L$  1.9–2.2 are located 7–10 km apart from the largest event with high horizontal uncertainty (3.1–9.0 km). We obtain an rms residual of 0.3 s and a mean horizontal error of 6 km (Table 1). The high station coverage can make some event locations more reliable, but the large uncertainty of  $Pn$  arrival times and velocity model, due to large event–station distance and weak signals, induces large location errors, especially for small events.

### DD relocation of the earthquake sequences using $dt$ derived from $Pn$ arrival times and waveform correlation

Using the DD earthquake relocation method (Waldhauser and Ellsworth, 2000), we relocated the earthquake sequences to constrain the small event location and reveal any lineament in the event locations. The  $Pn$  arrival times used for the single event location are utilized to obtain the  $dt$  of event pairs at common stations. We first searched for optimum event pairs to ensure stable solutions and adequate connectedness between events. We set the maximum event separation distance (also called interevent distance) of 10 km—about the event location uncertainty and spread, between event pairs to search a network of links between the events. We obtained 27 event pairs among the nine events. Each event link spans between a handful and over 50 stations, as shown in Figure S6. Final relocation by the DD method using phase data yields the six earthquakes (events 1, 3, 5, 6, 7, and 8) located close together as a cluster,

whereas three small events (2, 4, and 9) were not relocated (Fig. S7b). Their mean horizontal uncertainty and rms time residual are 5.0 km and 0.37 s, respectively.

We further utilized the WCC technique to examine if we can reduce location uncertainty with  $dt$  measured from the  $Pn$ -wave WCC. The WCC of the  $Pn$  waves with a correlation coefficient cutoff of 0.7 produced 67  $dt$  values from 27 event pairs. Although the relocation result using  $dt$  values from the phase data and WCC technique provides a coherent NW–SE distribution consistent with a nodal plane of the focal mechanism (Fig. S7c), location uncertainties are still high, and three smaller events are not relocated. Although the DD method has a weak depth resolution, the average focal depth of 10.45 km for six events is obtained (Fig. S7e,f).

## RELOCATION OF 2021 OFFSHORE GUNSAN EARTHQUAKES USING REGIONAL $Lg$ WAVE

In recent years,  $Lg$  wavetrain has been successfully used to relocate seismic events at regional distances when there is a lack of nearby stations (e.g., Schaff and Richards, 2004b; Schaff, Kim, et al., 2018; Schaff, Richards, et al., 2018; Han et al., 2024, among others). The core of the  $Lg$ -wave analysis is applying the WCC technique to determine the travel-time difference of the  $Lg$  wavetrain at common stations from closely located event pairs and then to relocate cluster of earthquakes using a reduced DD method by Schaff and Richards (2004b) derived from the original method of Waldhauser and Ellsworth (2000). The method is based on the fact that  $Lg$  waves correlate well in cases with similar focal mechanisms and event separation distances of less than  $\sim 1$  km at common stations. The effect of the unknown velocity structure can be reduced, similar to the original DD method. In contrast,  $Pn$  and  $Sn$  phases have short time windows to be used and usually low signal amplitudes at regional distances.

In the case of the 2021 Offshore Gunsan earthquakes, we have no seismic stations closer than 160 km, and characteristic regional seismic waves— $Pn$ ,  $Pg$ , and  $Sn$  are weak at nearly all stations, as discussed in the previous section. However,  $Lg$  waves are strong and predominant seismic signals on three-component records at all stations around the epicenter, ranging from 160 to 550 km, as shown in Figure 2. The time-bandwidth (TB) product is a product of time-window length and frequency bandwidth that is bounded by a lower and an upper frequency limit. According to previous studies (Harris, 1991; Schaff, Richards, et al., 2018), higher TB of  $>100$  will reduce cycle skipping due to noise signals, leading to reliable waveform cross-correlation. We obtain 123.2 for the TB product given the time window of 22.4 s for a median epicentral distance of  $\sim 300$  km and frequency bandwidth of 0.5–6 Hz. Hence, utilizing the  $Lg$  wave is ideally suited to analyze the earthquakes in the Yellow Sea. We employ the  $Lg$  WCC technique to relocate precisely the events to delineate these offshore earthquakes.

## Differential travel times of event pairs using $Lg$ wavetrain

We followed analysis methods given by Schaff and Richards (2004b) and Schaff, Richards, et al. (2018) to measure the  $dt$  of event pairs by cross-correlation of the  $Lg$  waves. Because  $Lg$  waves are the strongest on the transverse (T)-component data among the three-component records, we use T-component broadband records for  $Lg$  WCC. We took the following steps to process the records for WCC: (1) rotated N-S and E-W records into radial and T components using corrected orientation for borehole stations from KMA (Son et al., 2022); (2) filtered T-component records using fourth-order Butterworth band-pass filter with nominal cutoff frequencies at 0.5–5 Hz and 1–6 Hz for larger ( $M > 2.5$ ) and smaller ( $M < 2.5$ ) events, respectively; (3) windowed T-component records starting from  $Lg$ -wave arrivals with the apparent group velocity from 3.7 km/s ( $-5$  s) to 2.9 km/s ( $+5$  s) and allowed time lag of  $\pm 10$  s, based on the maximum separation distance of event pairs from the initial event locations (Fig. 1b); (4) obtained cross-correlation times with subsample precision by fitting to the parabolic function around the correlation peak (Deichmann and Garcia-Fernandez, 1992); and (5) used  $Lg$  waves with cross-correlation coefficient (Cc) higher than 0.35. We obtained 984 differential travel-time measurements for the 36 event pairs from nine events.

The  $Lg$  wavetrain on T-component records from all events at stations IJDB ( $\Delta = 204$  km, AZ = 112°) in the Korean peninsula and at RSH ( $\Delta = 248$  km, AZ = 300°) in eastern China are shown in Figure 3 to illustrate the remarkable similarity of the  $Lg$  wavetrain. Each trace is aligned relative to that of event 1. In each station,  $Lg$  waveforms from all events are overlaid at the bottom trace to show waveform similarities (Fig. 3). Although mean Ccs are 0.38 for IJDB and 0.44 for RSH; the large amplitude packets of signals (around 57–62 s at IJDB and 71–76 s at RSH) are well matched. These examples show the potential for high-quality estimation of the  $dt$  of event pairs by  $Lg$  waves in the regional distance. Even the events with low magnitude ( $M_L$  1.9–2.6) and high noise (events 2, 6, and 9) show reasonable waveform similarities and Cc values.

## Quality and uncertainties of differential travel-time measurements of $Lg$ wave

To ensure the quality of the measured  $dt$ , we examined the  $dt$  of each event pair and removed outliers. Schaff, Richards, et al. (2018) removed the outliers if their  $dt$  exceeded a preset threshold of the median of  $dt \pm 0.33$  s. This threshold of 0.33 s accounts for the travel-time difference between an event pair with a maximum nominal event separation distance of 1.0 km (calculated as 1.0 km/3.3 km/s = 0.30 s) and an acceptable correlation measurement error of 0.03 s. However, Schaff, Richards, et al. (2018) mentioned that it can be biased when the event pairs are separated larger than 1 km. We also found that it works for the event pairs with nearly even station

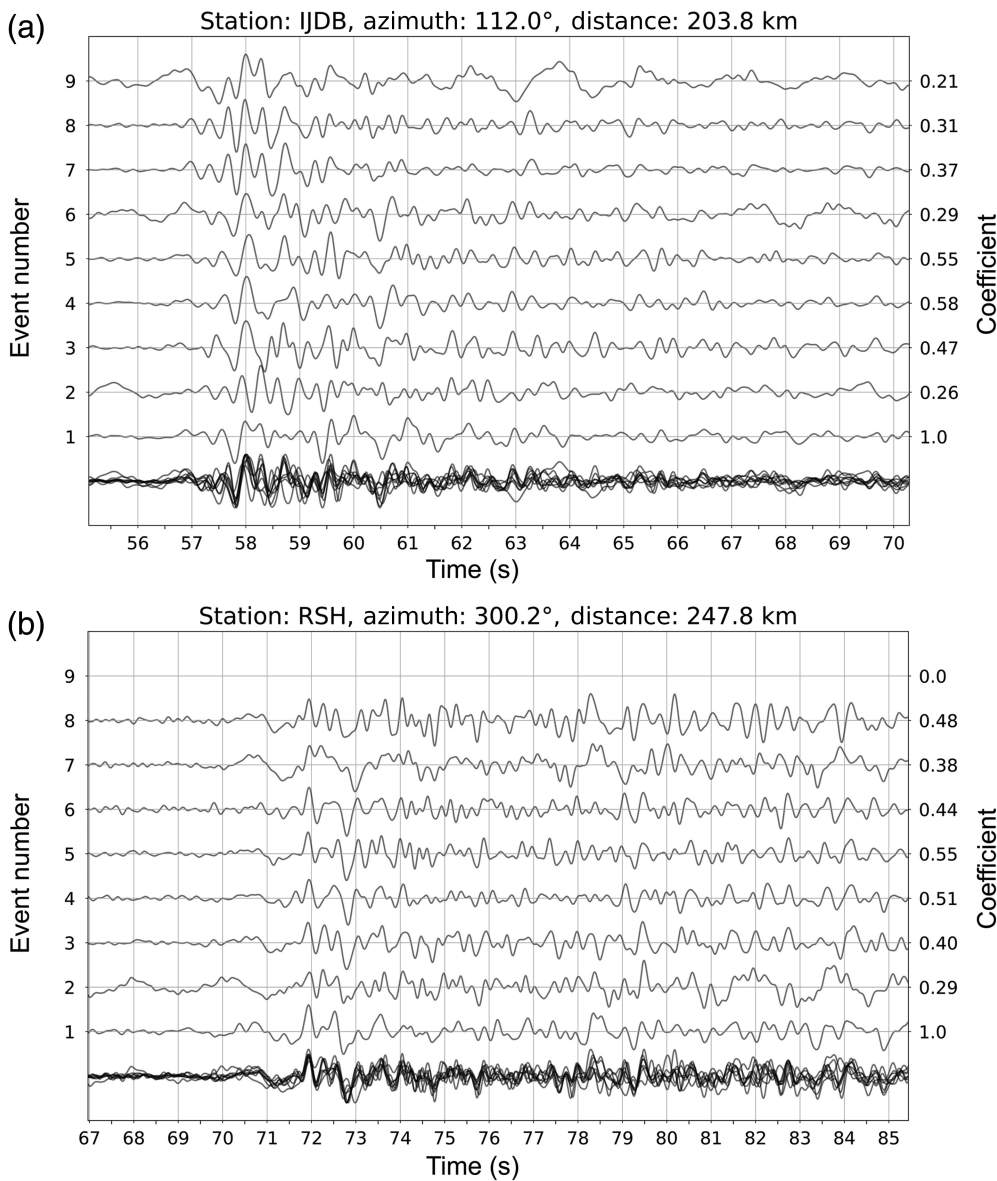


**Figure 3.**  $Lg$  wavetrain on the transverse-component records from nine events are plotted for two stations: (a) IJDB ( $\Delta = 203.8$  km, AZ = 112°) and (b) RSH ( $\Delta = 247.8$  km, AZ = 300°).  $Lg$  waves in the apparent group velocity window 3.7–2.9 km/s are filtered between 0.5 and 5 Hz and are aligned to event 1 for plotting. On each trace, the event ID is indicated at the beginning, and the Cc value with respect to the reference trace (1) is indicated at the end of each trace. At each station, all traces are plotted on top of each other at the bottom to illustrate the waveform similarity. At RSH, the record from event 9 is not available. Note that the early portion of the  $Lg$  wavetrain from events 1–6 and 7–8 are dissimilar from each other.

azimuthal distribution, but for event pairs with uneven station distribution, the median is heavily biased toward the cluster of stations. This is true for most event pairs of the Gunsan earthquake sequences where there are gaps due to the sea in the N–S direction and denser station distribution in the southern Korean peninsula in the eastern azimuth (see Fig. 1a, Fig. S1).

We have  $Lg$  observations from enough stations, and the observed  $dt$  from many event pairs show well-defined sinusoids around station azimuth, as shown in Figure 4. We obtained a robust model to fit the observed  $dt$  data of the event pair better

(see Text S1). Usually, the best  $dt$  is obtained for event pairs with both events similarly sized (see Fig. 4, Figs. S8 and S9), that is, with a magnitude difference of less than 0.3 ( $\Delta M \sim 0.3$ ;  $\Delta M = M_{L1} - M_{L2}$ ), and both events are adequately sized ( $M_L > 3.0$ ) so that signal-to-noise ratios (SNRs) are high. This characteristic is also maintained in different components (Fig. S10). Obviously, event pairs with large magnitude differences and weak event pairs ( $M_L < 2.5$ ) produced  $dt$  with large scatter and low Cc values (see Figs. S8 and S9).

#### DD relocation method using $Lg$ wave

Under the straight path assumption for  $Lg$ -wave propagation, the DD equation is reformulated analytically, as Schaff and Richards (2004b) showed. By fixing the focal depth, Schaff and Richards (2004b) formulated the DD equation for centroid epicenter coordinates  $x$  and  $y$ , and centroid time  $\tau$ . If we let local station coordinates be  $x_s$  and  $y_s$ , then the distance,  $D$ , between the epicenter and station is;  $D = \sqrt{(x - x_s)^2 + (y - y_s)^2}$ . If we use an  $Lg$ -wave velocity,  $V_{Lg}$ , for its straight path, then the travel time of  $Lg$  wave,  $t$ , is,  $t = D/V_{Lg}$ , in which  $V_{Lg} = 3.3$  km/s is adequate because most energy in the  $Lg$ -wave packet travels with this

apparent group velocity (see Fig. 2). The partial derivatives of travel time can be written analytically due to the straight ray path as  $\partial t/\partial x = (x - x_s)/(V_{Lg} \times D)$  and  $\partial t/\partial y = (y - y_s)/(V_{Lg} \times D)$ . These equations are the same as those given by Schaff and Richards (2004b) and Son *et al.* (2015).

The solution is found through an iterative application of the conjugate gradient algorithm, the least squares method (Paige and Saunders, 1982), as used in the hypoDD program (Waldbauer, 2001). We iterated this algorithm until it reached the preset maximum number of iterations with two given

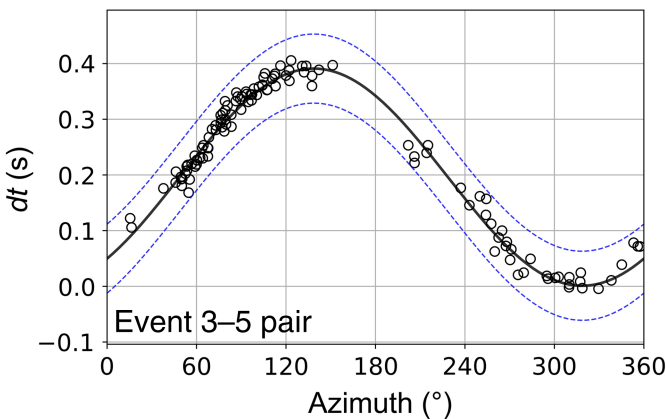


**Figure 4.** Observed differential travel times ( $dt$ ) of event pair 3–5 plotted against station azimuth (circles). The  $dt$  for a pair of events is expected to show a sinusoid as a function of station azimuth. The distance between the event pair determines the maximum height of the sinusoid, whereas the median or mean of all  $dt$  is related to the centroid time difference. The solid curve is the calculated sinusoid of station azimuth plus azimuth from event 3 to event 5 and is represented by a function:  $-0.173 \sin(AZ + 137^\circ) + 0.176$ . The blue dashed lines are plus or minus half the standard deviation ( $\sigma/2 = 0.067$  s) of the observed  $dt$ . Event pair 3–5 has an event separation distance of 0.6 km, and the observed  $dt$  are distributed around the calculated  $dt$  within  $\pm 0.067$  s. The root mean square (rms) differential travel-time residual [ $dt^{\text{obs}} - dt^{\text{cal}}$ ] is 0.024 s, suggesting consistent  $dt$ . The color version of this figure is available only in the electronic edition.

parameters. The first parameter is a threshold for time residual, which is used to remove observed differential travel-time values that exceed the threshold in each iteration (typically 3–6 times the standard deviations; Waldhauser and Ellsworth, 2000). The second parameter is the interevent distance cut, which is used to remove event pairs that exceed the cutoff distance during iterations. It is used to reduce the influence of distant event pairs that might deviate from the common path assumption. We allowed an interevent distance cutoff of 2 km.

## Epicentral relocation results and its uncertainties

We relocated all nine events using  $dt$  from  $Lg$ -wave correlations. We obtained an rms  $dt$  residual value of 0.015 s—a factor of 24 smaller than the rms time residual ( $0.370 \pm 0.058$  s) from the DD relocation with the  $Pn$  phase data (Fig. S7). In the final iteration, 649  $dt$  data on 15 pairs were used. The connectedness of event pairs in relocation is depicted in Figure S11. The events are well connected with a maximum interevent distance of 2 km in the final iteration of the relocation. The relocated epicenters are realigned to the absolute location of reference event 1, which is the largest event and has the smallest location uncertainty (Table 3, Fig. 5a).

We next estimated the horizontal uncertainties of the relocated events using the bootstrap error estimation. Specifically, we randomly sampled the  $dt$ , with replacement, from 137 stations. We then relocated the earthquakes for 10,000 bootstrapped samples while removing centroid perturbation. The standard error was estimated to the distribution of epicenters of each event using the 95% confidence interval, which corresponds to  $2\sigma$ . The mean semimajor axis is  $0.58 \pm 0.18$  km, and the mean semiminor axis is  $0.32 \pm 0.14$  km (Fig. 5b). Among events, event 9 has the largest error of  $\sim 0.9$  km due to weak signals from this small-magnitude event and no data coverage from stations in the western half of the coverage. Nonetheless, the rms time residual and horizontal uncertainty are improved  $\sim 24$  and 17 times better than the catalog relocation, respectively. Therefore, we consider our relative location estimates for the 2021 earthquake sequences to be of adequate quality based on error ellipses, small rms residuals, and overall waveform fits.

## SOURCE CHARACTERIZATION USING $Lg$ WAVE: EGF APPROACH

The successful relocation of two earthquake sequences in January and December 2021 using regional  $Lg$  waves raised some questions on why the two sequences are about 11 months apart temporally, while the two sequences align along a fault

TABLE 3  
Relocated by Epicentral Double-Difference (DD) and Error Ellipse from Bootstrap Analysis

ID	Date (yyyy/mm/dd)	Time (UTC) (hh:mm:ss.ss)	Latitude (°N)	Longitude (°E)	M ( $M_L$ )	Az (°)	Major (km)	Minor (km)	rms (s)
1	2021/01/18	18:21:29.14	35.80985	123.99255	4.6	30.5	0.460	0.256	0.019
2	2021/01/19	13:58:30.26	35.80295	124.00175	1.9	27.5	0.710	0.304	0.019
3	2021/01/21	21:01:49.28	35.81385	123.98055	3.2	29.2	0.425	0.225	0.017
4	2021/01/29	13:34:54.25	35.81565	123.96725	2.6	28.7	0.437	0.224	0.015
5	2021/02/04	01:56:19.62	35.80955	123.98525	2.9	29.0	0.427	0.224	0.016
6	2021/03/09	17:56:23.40	35.81075	123.97765	1.9	29.1	0.429	0.225	0.016
7	2021/12/03	12:08:23.16	35.79555	124.01465	4.5	31.2	0.711	0.392	0.014
8	2021/12/03	15:18:10.10	35.79205	124.02155	3.4	29.9	0.706	0.343	0.017
9	2021/12/04	00:30:17.07	35.79405	124.01955	2.2	77.0	0.899	1.299	0.023

Epicentral DD locations are adjusted by moving relative to the event 1 location from the HYPOINVERSE. Az, azimuth; M, magnitude; Major, semimajor axis; Minor, semiminor axis of the error ellipse in kilometers; and rms, root mean square differential travel-time residuals in the DD location.

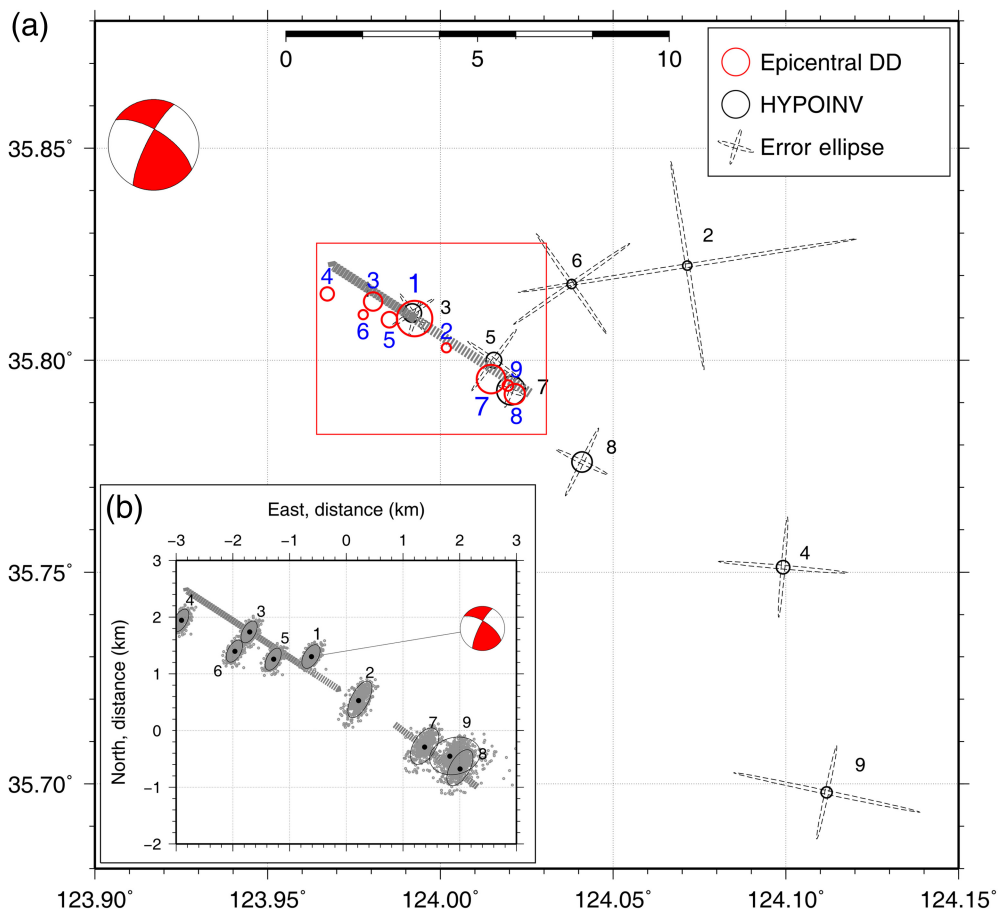


**Figure 5.** Map view of the earthquake sequences. (a) Absolute locations from HYPOINVERSE are plotted as solid circles with their error ellipses, whereas the epicentral DD relocations are plotted as red circles. The event 1 cluster roughly aligns along the strike direction of a nodal plane striking west-northwest (WNW) ( $303^\circ$ ) of the focal mechanism. The earthquakes of the December 2021 sequence are also aligned along the nodal plane, striking WNW as in the January sequence. The two sequences appear parallel, but they may not be on a continuous single-fault plane. A red rectangle marks the area of panel (b). (b) Epicentral DD relocation of six earthquakes of the January 2021 sequence (events 1–6) and three earthquakes of the December 2021 sequence (events 7–9) forms separate clusters around the main events of the sequences. Events 1 and 7 are separated by about 2.5 km. The event pair produced about 40  $dt$  fairly well distributed around azimuth (see Figs. S10–S13). However, the  $dt$  is not used in the final relocation because we preset a maximum event separation distance of 2 km (WDCC) in the final iteration of the relocation. The color version of this figure is available only in the electronic edition.

trace that strikes SE ( $\sim 125^\circ$ ) and separated by about 2.5 km. We next characterize the source property of the two sequences in more detail using regional  $Lg$ -wave observations in an attempt to find some clue on the above questions.

$Lg$  wave has been used to estimate the source spectrum corner frequency of small earthquakes in eastern North America using EGF analysis (e.g., Shi *et al.*, 1996). We employed the EGF approach with observed  $Lg$  waves to determine the corner frequency of the two main events. For the January 2021  $M_L$  4.6 earthquake, event 5 ( $M_L$  2.9, Table 1, Fig. 5) is the best EGF event among the five aftershocks because it is the closest (0.66 km) and shows good waveform similarity with the main event. Event 3 is slightly larger ( $M_L$  3.2) but located farther

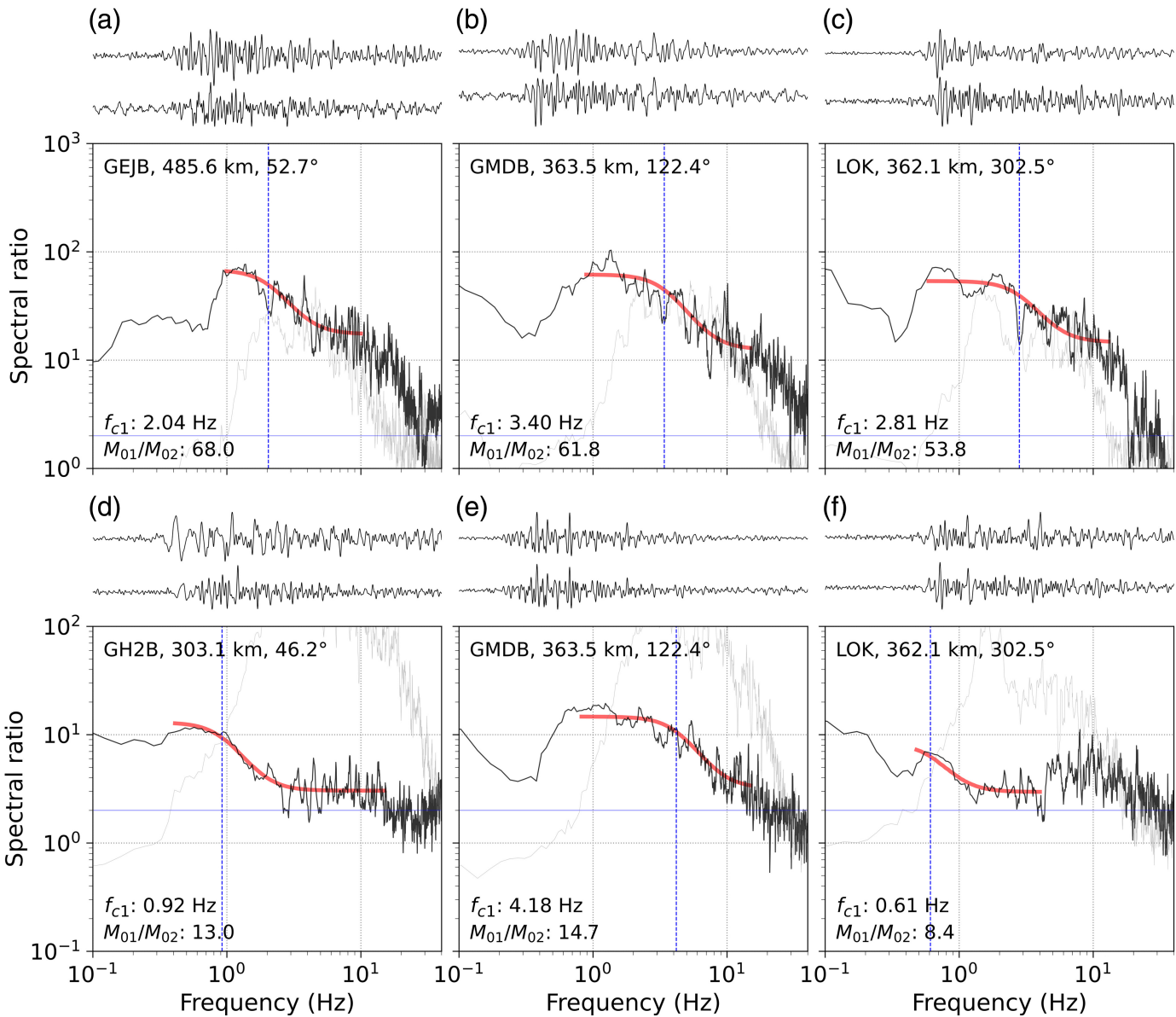
away from the mainshock ( $\sim 1.17$  km). For the December 2021  $M_L$  4.5 earthquake, event 8 ( $M_L$  3.4) is a good EGF event since it is close ( $\sim 0.74$  km) and generated decent signals with high SNR.

We used the  $Lg$  waves on the T component in the group velocity window from 3.7 km/s ( $-5$  s) to 2.9 km/s ( $+5$  s) for the EGF analysis.  $Lg$ -wave signals of the EGF pairs are multitapered to calculate the displacement amplitude spectra (e.g., Prieto *et al.*, 2009). We calculated the noise spectra with the same time-window length as the  $Lg$ -wave window that ends 5 s before the  $Pn$  arrival with  $\sim 8$  km/s apparent group velocity (see Fig. 2). To ensure the quality of the data, we used only signal amplitude spectra that were greater than two times the noise amplitude spectra. The stations for which spectra passed the noise threshold are mainly located in southwestern Korea and the Shandong peninsula in China (Fig. S1a).

We modeled the deconvolved spectral ratio by assuming a  $\omega^2$  source model (Aki, 1967), parameterized with the seismic moment ratio and corner frequencies. The spectral ratio,  $R(f)$ , can be fit by a spectral source model (Brune, 1970, 1971; Boatwright, 1980),

$$R_{12}(f) = U_1(f)/U_2(f) = (M_{01}/M_{02}) \times [(1 + (f/f_{c2})^{2\gamma})/(1 + (f/f_{c1})^{2\gamma})]^{1/\gamma}, \quad (1)$$

in which the subscript 1 denotes the target main event; 2 denotes the EGF event;  $f$  is the frequency;  $U(f)$  is the observed  $Lg$ -wave displacement amplitude spectrum;  $f_c$  is the corner frequency;  $M_0$  is the seismic moment; and  $\gamma$  is the constant controlling the shape of the corner frequency. We selected constant  $\gamma = 2$  (Boatwright, 1980) in equation (1) that yields the best fit to the observed ratio (compare with  $\gamma = 1$  for parameterization by Brune, 1970, 1971). We constrained the seismic moment ratio and corner frequencies that minimized

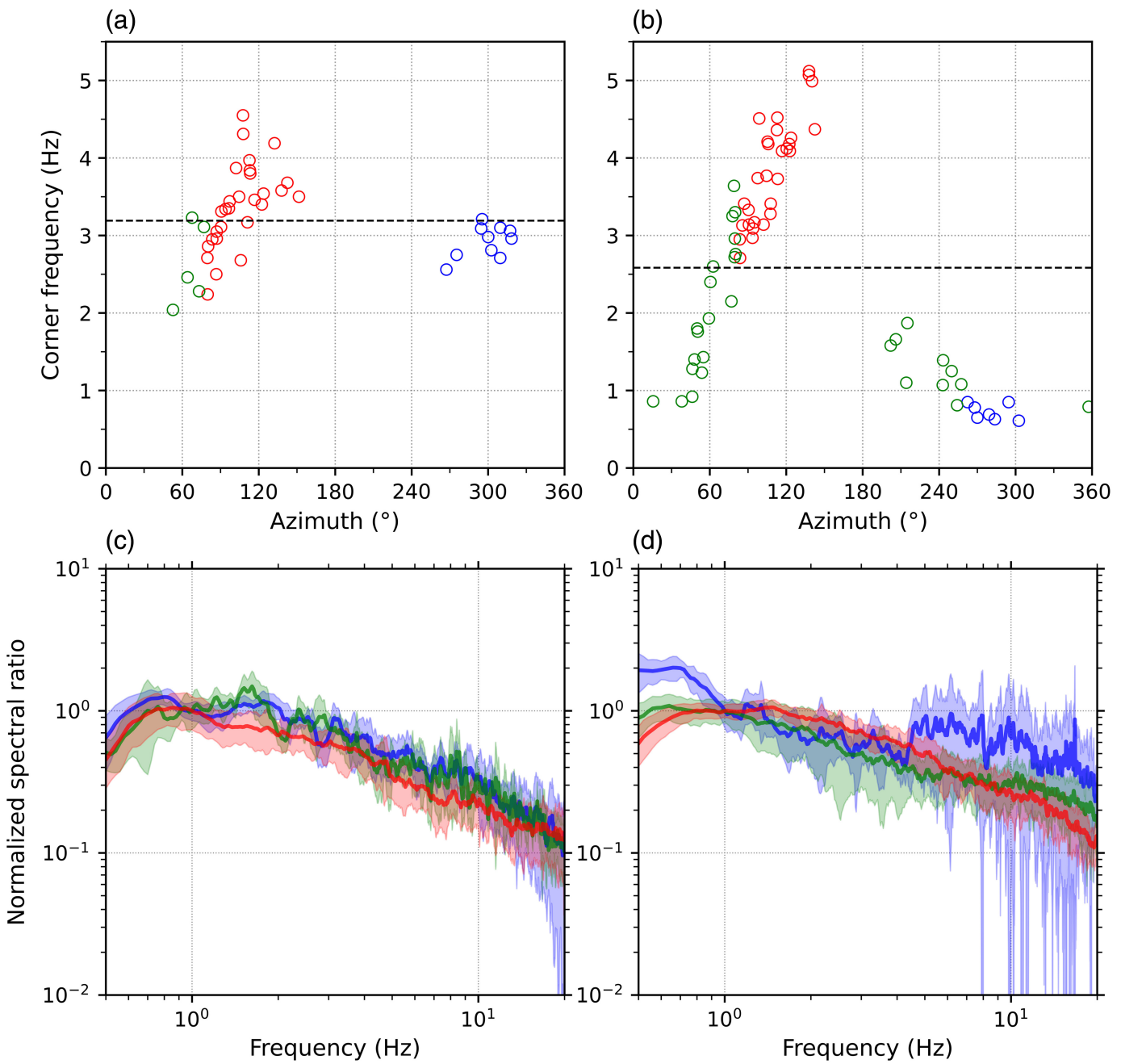


the variance between the observed ratio and model spectra by a grid search (Fig. 6).

Selected spectral ratios and fitted model spectra are plotted in Figure 7. The estimated corner frequency of the target mainshock ranges from 2.04 to 4.55 Hz with a mean value of  $3.19 \pm 0.55$  Hz from 43 stations for event 1. The corner frequency shows some dependency on station azimuth, as shown in Figure 7a. Although there are large gaps in the azimuthal coverage, the corner frequency increases with azimuth between  $\sim 50^\circ$  and  $150^\circ$  (Fig. 7a) and the highest value toward ESE (about  $120^\circ$ ), which is the strike of the presumed fault trace (Fig. 7a), suggesting that it is the forward direction of the rupture. The corner frequency in the opposite direction ( $\sim 303^\circ$ ) shows an average value ( $\sim 3$  Hz; see Fig. 7a). Unfortunately, we could not estimate the corner frequency at stations on both sides of normal to the fault-strike direction due to low SNR. These stations are also normal to the rupture plane dipping steeply ( $65^\circ$ ) to the NE (Table 2).

**Figure 6.** (a–c) Deconvolved spectral ratio of the empirical Green's function (EGF) pair 1–5 from three stations at selected azimuth are plotted for comparison. The observed spectral ratio is plotted with black lines, and the fitted model spectrum is plotted with red solid lines at each station. (a) Normal to the strike direction. (b) Strike direction on east-southeast (ESE). (c) Strike direction on WNW. The used  $Lg$  waveforms are plotted above each spectral ratio. Each blue-dotted vertical line indicates the corner frequency of the target event determined in each station. A blue-thin horizontal solid line indicates a spectral ratio of 2. A light gray line represents signal-to-noise ratio (SNR). Each frame indicates the station code, distance, azimuth, corner frequency, and moment ratio. (d–f) The deconvolved spectral ratio of the EGF pair 7–8 from three stations at selected azimuth is plotted for comparison. Other notations are the same as the panels (a–c). The color version of this figure is available only in the electronic edition.

For event 7, the estimated corner frequency ranges from 0.61 to 5.12 Hz with a mean of  $2.58 \pm 1.36$  Hz from 65 stations (Fig. 7b). The corner frequency increases with azimuth from  $\sim 38^\circ$  to  $143^\circ$  at a rate much faster than event 1. These stations



are all in the Korean peninsula (Fig. 7b). At stations in eastern China, the corner frequency decreases up to the opposite direction ( $\sim 303^\circ$ ). Hence, there is a sense of narrower source duration toward the ESE fault-strike direction, implying a strong rupture directivity. However, the spectral ratios at stations at an azimuth greater than  $240^\circ$  in eastern China are poorly defined, as shown in Figure 6f. A dozen spectral ratios observed at azimuth range  $240^\circ\text{--}303^\circ$  have a lack of energy at low frequencies, but the ratio bursts into high amplitude at frequencies higher than  $\sim 5$  Hz (Figs. 6f and 7d).

### Rupture directivity and properties

To characterize the rupture processes of the sources, the spectral ratios were stacked for stations along the ESE strike

**Figure 7.** (a) Estimated source corner frequencies of event 1 plotted against azimuth by circles. The red, green, and blue circles represent the source corner frequencies in each station within rupture direction  $\pm 45^\circ$ , opposite direction  $\pm 45^\circ$ , and normal direction  $\pm 45^\circ$  azimuth, respectively. A dashed line indicates the average corner frequency value. (b) Estimated corner frequencies of event 7. (c) Stacked spectral ratios of event 1–5 pair. The thick red, blue, and green lines represent the averaged stacked spectral ratio within rupture directions same as panels (a) and (b). All stacked spectral ratios are normalized by spectral ratio at 1 Hz. The shaded area shows the standard deviation range of each stacked spectral ratio. (d) Spectral ratios of event 7–8 pair. The color version of this figure is available only in the electronic edition.

( $123^\circ \pm 45^\circ$ ), normal to strike ( $33^\circ \pm 45^\circ$  and  $213^\circ \pm 45^\circ$ ), and along WNW-strike ( $303^\circ \pm 45^\circ$ ) directions, and their scatters were estimated. Three stacked spectral ratios with scatter are normalized by spectral ratio at 1 Hz and shown in Figure 7c,d.

The spectral ratios,  $R(f)$ s, from the EGF pair show a consistent shape for the  $M_L$  4.6 event over a wide range of azimuth (Fig. 7c) with slightly higher corner frequency values at stations toward the strike direction ( $123^\circ$ ), which gradually increase from an azimuth of  $\sim 60^\circ$  toward  $\sim 120^\circ$  (Fig. 7a). In contrast, the source spectral ratios for the December 2021  $M_L$  4.5 event show stronger variation along the azimuth than event 1, as shown by the three stacked spectral ratios in Figure 7d. The stacked ratios along the strike direction (thick red line) show higher amplitude at high frequencies than those along the opposite direction ( $\sim 307^\circ$ ). We note that the sudden increase of the ratio starting at 5 Hz along the opposite direction ( $\sim 307^\circ$ ) might be due to the different fall-off rates of two events and/or double corner frequencies (Uchide and Imanishi, 2016; Yoshimitsu et al., 2019). However, the corner frequency of the target event can be well-defined using a limited frequency band before the jump (Yoon et al., 2019). Therefore, we used spectral ratio using a more limited frequency band to estimate corner frequency without a jump (see Figs. S12 and S13).

Assuming a circular fault model, we calculate the source radius,  $r_0$ , using the mean corner frequency and using the equation,  $r_0 = \frac{k\beta}{f_c}$ , in which  $\beta$  is the shear-wave velocity near the source (3.6 km/s in this study), and  $k = 0.37$  assuming the model of Brune (1970, 1971). We obtain the source radius of 0.41 km with the average  $f_c = 3.19$  Hz for event 1, and  $r_0 = 0.5$  km with the average corner frequency of  $f_c = 2.58$  Hz for event 7. The stress drop ( $\Delta\sigma$ ) may be calculated using the formula  $\Delta\sigma = (7/16)(M_0/r_0^3)$  of Eshelby (1957) with the calculated source radius and the seismic moment obtained from moment tensor inversion given in Table 2. The stress drops are 84.4 and 8.3 MPa for event 1 and event 7, respectively.

However, we note that our assumption of the circular fault model here is not consistent with our observations of the rupture directivity of these two earthquakes. Despite uneven azimuthal coverage of the spectral ratios and the estimated source corner frequencies of the target mainshocks, we were able to characterize and discern the rupture directivity of these events with confidence by employing the EGF approach using regional  $Lg$ -wave observation. Interpreting further details of the source is not warranted, given the limitation of  $Lg$  waves leaving the source with narrow takeoff angles.

## DISCUSSION

### Maximum interevent distance for $Lg$ -wave Cross-Correlation

Previous studies used  $Lg$ -wave cross-correlation (CC) successively for detecting seismic events, finding repeating earthquakes, and relocating clusters of events. For instance, Schaff and Richards (2004b) utilized  $Lg$ -wave correlation measurements

recorded at five stations in epicentral distances between 500 and 1000 km to relocate for  $\sim 90$  events in Xiuyan, China; Schaff, Kim, et al. (2018) precisely relocated 13 small events near the North Korean nuclear test site recorded at 11 stations with a mean epicentral distance of  $\sim 410$  km, and the maximum station gap of  $153^\circ$ ; and Schaff, Richards, et al. (2018) performed epicentral relocation with a sparse network of stations and broad area using  $Lg$ -wave CC data in western China with a station gap of  $205^\circ$  and mean distance of 898 km. In these studies,  $dt$  from  $Lg$ -wave CC measurements are suggested to be limited to the maximum interevent distance of 1 km for the event pairs as the waveform similarities deteriorate as the interevent distance increases (e.g., Slinkard et al., 2016).

In this study, we attempted to relocate nine small-to-moderate earthquakes that occurred in the Yellow Sea using  $Lg$ -wave correlation measurements. Unlike many previous studies, we have waveform data from over 149 stations in the distance range from 160 to 550 km with a mean distance of  $\sim 300$  km and have decent azimuthal coverage with an average maximum azimuthal station gap of  $\sim 100^\circ$  but only nine events to relocate. In the Quality and uncertainties of differential travel-time measurements of  $Lg$  wave section, we showed that our  $Lg$ -wave differential travel-time measurements are independent of the distance, and the scatter of  $dt$  among the three components is within  $\pm 0.05$  s (Fig. S10).

The mean interevent distance is  $1.04 \pm 0.50$  km for 16 linked pairs ranging from 0.29 to 1.89 km (see Fig. S11). We find that the interevent distance for  $Lg$ -wave correlation measurements can be extended up to 2.5 km, as shown in Figure 5b and Figure S6b. We were able to extend the maximum interevent distance for event pair 1–7 up to 2.5 km because of the fact that two events of the pair have the same focal mechanism and focal depth, as well as  $Lg$  wavetrain on most stations have high SNR because two events are the strongest, and have similar magnitude ( $M_L$  4.6 and 4.5). The event pair produced about 41  $dt$ , fairly well distributed around the azimuth with a maximum azimuthal gap of  $\sim 60^\circ$  (see Fig. S9b). Therefore, we suggest that the interevent distance can be greater than 1 km and can be extended twice that distance, that is, 2 km, for event pairs with favorable conditions for  $Lg$  WCC measurements, such as common focal mechanism and depth, similar size ( $\Delta M_L < 0.3$ ), with sufficient SNR ( $M > 3.0$ ), these may be the attribute for an ideal  $Lg$  correlation pair.

### Implications to regional seismogenic faults and tectonic activities

The consistent P-axis azimuth might suggest that the region is under a uniform stress field (e.g., Morris et al., 1996; Uchide et al., 2022). The P-axis azimuth of the two mainshocks of the 2021 Gunsan sequences is  $\sim 78^\circ$  (Table 2), which is similar to the P-axis azimuth of  $\sim 70^\circ$  for earthquakes that occurred in the Yellow Sea and the Korean peninsula (Fig. 1a, Fig. S14) (e.g., Rhee and Kim, 2010; Hong and Choi, 2012). This may indicate

that the compressional stress currently acting on the Gunsan basin is controlled by the same tectonic stress affecting the surrounding region.

The P-axis plunge of the two mainshocks is  $\sim 5^\circ$  (Table 2), which is also similar to the earthquakes in the Yellow Sea and the Korean peninsula, and indicates that strike-slip faults are dominant (Fig. 1a, Fig. S14). However, earthquakes occurring in the Qianliyan uplift region, located north of the Gunsan basin, are associated with normal faults and have a P-axis plunge of  $\sim 56^\circ$  (Fig. 1a, Fig. S14). The presence of normal faults has been suggested to be related to the Jurassic collision zone (Hong and Choi, 2012), but there is still debate about the location of its boundary (e.g., Yin and Nie, 1993; Chough *et al.*, 2000; Oh, 2006; Chang and Zhao, 2012; Choi *et al.*, 2015). The P-axis plunge measured in the Gunsan basin might indicate that the boundary of the Jurassic collision zone is located north of the Gunsan basin. However, since our study focused on two closely located earthquake sequences, the results are limited to seismogenic structures in the Gunsan basin. Further investigation into the seismogenic faults and rupture characteristics throughout the Yellow Sea is necessary to understand a more comprehensive relationship between seismicity and regional tectonic activities.

### Different rupture directivity of two sequences

Azimuthal variation of spectral ratio can be used to observe rupture directivity (Kane *et al.*, 2013). In this study, three directions of stacked spectral ratios of event 1 show obscure direction (Fig. 7c). The standard deviation of observed corner frequency is relatively small (Fig. 7a). Although there is a large azimuthal gap in the observed corner frequencies, this corner frequency variation with azimuth may suggest the rupture propagated slightly toward SE ( $123^\circ$ ). Therefore, we may suggest that event 1 can be considered asymmetrical circular or bilateral rupture. In contrast, event 7 has strong azimuthal variation in stacked spectral ratio and observed corner frequency (Fig. 7b). This variation with azimuth indicates that the rupture propagated strongly toward the SE ( $127^\circ$ ). We suggest that event 7 can be considered as a unilateral rupture.

The rupture directivity can also be observed in the ground motion. For instance, Boatwright (2007) showed rupture directivity for seven  $3.5 \leq M \leq 4.1$  events in San Ramon using peak ground motion; Seekins and Boatwright (2010) also used peak ground motion to observe rupture directivity of 47 moderate earthquakes ( $3.5 \leq M \leq 5.4$ ) in northern California. We observed similar azimuthal variation in the displacement spectrum of stations of two mainshocks (Fig. S15). At the rupture direction, the displacement spectral amplitudes of event 7 are as high as those of event 1 in the high-frequency range ( $\sim 3$  Hz), despite a similar amplitude gap in the low-frequency plateau (0.1–0.5 Hz) due to magnitude difference. Conversely, stations located in the opposite direction of the rupture for event 7 exhibit much lower amplitudes.

The strong rupture directivity of  $M_L$  4.5 event leads to the large difference in observed corner frequency along azimuth (Fig. 7b). The standard deviation of the observed corner frequency of event 7 is 1.36 Hz, whereas event 1 has about 2.5 times smaller standard deviation (Fig. 7a,b). Considering the standard deviation, the rupture radius of event 7 can be changed to 0.33 or 1.1 km. These radii yield stress drops of 29.6 or 0.9 MPa. Kaneko and Shearer (2014) suggested that the limited azimuthal coverage will likely bias corner frequency. Our results show that the limited azimuthal coverage can produce largely biased average corner frequency and have high uncertainty, especially in unilateral rupture.

### High stress drop of $M_L$ 4.6 mainshock

Despite the limited azimuthal coverage, the  $M_L$  4.6 event exhibits lower uncertainty due to its circular or bilateral rupture propagation. Notably, it exhibited a higher stress drop (84.4 MPa) compared to other earthquakes occurring in and around the Korean peninsula, even considering different methods and assumptions. For instance, in the southern part of the Yellow Sea region, Park *et al.* (2012) reported a stress drop of 1.2–2.0 MPa for an  $M_w$  4.6 event, suggesting a potentially different tectonic setting than the Korean peninsula, which typically experiences higher stress drops for intraplate earthquakes. Previous studies have reported stress drops of moderate earthquakes exceeding 10 MPa in the Korean peninsula (e.g., Kim *et al.*, 2010, 2023; Kim and Kim, 2014; Uchide and Song, 2018; Chai *et al.*, 2020) and eastern North America (e.g., Viegas *et al.*, 2010; Wu and Chapman, 2017), which are located at all under the intraplate setting, attributing these high values to high frictional strength due to long quiescent periods. In addition, Onwuemeke *et al.* (2018) suggested that earthquakes that occur on less-matured faults have higher stress drops which indicate higher fault strengths. The higher stress drop of the  $M_L$  4.6 event than other events in the aforementioned studies may also represent the higher frictional strength of the fault.

We note that the  $M_L$  4.6 event is situated in an intraplate region and has undergone an extensive quiescent period, spanning at least over 50 yr (see Fig. 1a). This prolonged quiescent time enhances fault strength by increasing the contact area with lower slip rates (Scholz *et al.*, 1986). Other factors contributing to a high stress drop include chemical/hydrothermal healing and elevated fault roughness. Tenthorey and Cox (2006) demonstrated through rock experiments that hydrothermal healing consolidates and strengthens the fault-damaged zone. Intraplate faults may exhibit higher fault roughness than interplate faults due to less-matured asperity (larger contact area) and less accumulated slip (Scholz *et al.*, 1986). Numerical simulations conducted by Kato (2009) highlighted the difference in stress drop between intraplate and interplate asperities, demonstrating a  $\sim 50\%$  higher stress drop in asperities representing intraplate earthquakes.

## CONCLUSIONS

Regional  $Lg$ -wave observations are used to precisely relocate epicenters of two 2021 earthquake sequences in the central region of the Yellow Sea.  $Lg$  WCC technique is employed to measure the differential travel time of event pairs for the DD earthquake relocation method with the maximum interevent distance up to  $\sim 2.5$  km for nine earthquakes in two event sequences. The results of relocation reveal that earthquakes of January and December 2021 sequences align along WNW–ESE-trending lineament of  $\sim 6$  km, consistent with a nodal plane striking  $303^\circ$ . It points to the NW–SE-trending left-lateral strike-slip fault as the seismogenic fault in the Gunsan basin region, where no prior significant earthquakes have been reported. Their P-axes are similar to the overall Yellow Sea and Korean peninsula, indicating that the compressional stress currently acting on the Gunsan basin is controlled by the same tectonic stress affecting the surrounding region. This is one of the first studies of earthquakes in the central Yellow Sea, in which earthquakes are precisely relocated to manifest a causative fault for the significant earthquake.

Based on epicentral relocation results, we determined the source spectrum corner frequency of the two mainshocks of the sequences by employing the EGF analysis. The corner frequencies of the two mainshocks show clear azimuthal variation, in that corner frequencies increase with azimuth from  $\sim 60^\circ$  to  $150^\circ$ , suggesting that rupture has propagated toward the SE on the rupture plane striking  $\sim 125^\circ$ , whereas the corner frequencies are quite low along the opposite direction ( $\sim 305^\circ$ ). Two mainshocks of the sequences show distinct rupture processes, event 1 ( $M_L$  4.6) exhibits weak asymmetrical bilateral or circular rupture, whereas event 7 ( $M_L$  4.5) exhibits a sense of unilateral rupture. Assuming a circular rupture model, the mean event corner frequency of the  $M_L$  4.6 mainshock yields a stress drop of 84 MPa. Such a high stress-drop value of the  $M_L$  4.6 event may indicate a higher frictional strength due to a long quiescent period in the Gunsan basin region and/or less-mature asperities on the seismogenic fault in the Yellow Sea.

## DATA AND RESOURCES

Waveform data of broadband seismometers of the Korea Meteorological Administration (KMA) were downloaded from the National Earthquake Comprehensive Information System website (<https://necis.kma.go.kr>) upon approval. Waveform data from open stations of KMA (network code: KS) is obtained from Incorporated Research Institutions for Seismology Data Management Center (IRIS-DMC) ([http://ds.iris.edu/SeismiQuery/by\\_network.html](http://ds.iris.edu/SeismiQuery/by_network.html)); non-open stations of KMA network is acquired through written requests. Waveform data of broadband seismometers of the China National Seismic Network were provided by the Data Management Centre of China National Seismic Network at the Institute of Geophysics (SEISDMC, doi: [10.11998/SeisDmc/SN](https://doi.org/10.11998/SeisDmc/SN)), China Earthquake Administration, and not all the data are publicly available (Zheng *et al.*, 2010). Earthquake catalogs of the 2021 Gunsan earthquake sequences and past seismicity (1976–2023) in Korea were accessed from

KMA online catalog (<https://www.weather.go.kr/w/ejk-vol/search/korea.do>), Global Centroid Moment Tensor (Global CMT) webpage (<https://www.globalcmt.org>) and International Seismological Centre (ISC) online bulletin (doi: [10.31905/D808B830](https://doi.org/10.31905/D808B830); <http://isc.ac.uk/iscbulletin/search/catalogue/>). The authors used Seismic Analysis Code (<https://ds.iris.edu/ds/nodes/dmc/software/downloads/sac/>), ObsPy (<https://docs.obspy.org>), Generic Mapping Tools (version 6.4.0.; <https://www.generic-mapping-tools.org>), and Python library Multitaper (<https://github.com/gaprieto/multitaper/>). Earthquakes are individually located using the computer code HYPOINVERSE (<https://www.usgs.gov/software/hypoinverse-earthquake-location>). Earthquakes are relocated using the computer code hypoDD ( $\sim$ <https://www.ledo.columbia.edu/~felixw/hypoDD.html>). All websites were last accessed in April 2024. The supplemental material includes descriptions of outliers in  $dt$  data constraining using sinusoid. The document also contains 15 figures and one table that supplement the results presented in the article.

## DECLARATION OF COMPETING INTERESTS

The authors acknowledge that there are no conflicts of interest recorded.

## ACKNOWLEDGMENTS

This study was supported by the Brain Pool Program of the National Research Foundation (NRF) of Korea (Grant Number 2020H1D3A2A02047949). J. Y. Park and Y.H. Kim acknowledge funding support from NRF (2022RIA2C1003006 and 2022RIA5A1085103). X. Shen acknowledges funding support from the National Natural Science Foundation of China (Grant Number 42230305) and Guangdong Province Introduced Innovative R&D Team (2017ZT07Z066). W.-Y. Kim received support from the Consortium for Monitoring, Technology, and Verification under the Department of Energy National Nuclear Security Administration, United States, Award Number DE-NA0003920. The authors would like to thank the operators of the seismographic networks who provided waveform data in a timely fashion: KMA & KIGAM, Korea, and China National Seismic Network. The authors acknowledge valuable comments and suggestions from Editor-in-Chief Martin Mai, Associate Editor Shengji Wei, and anonymous reviewers that helped improve the clarity of the article.

## REFERENCES

- Aki, K. (1967). Scaling law of seismic spectrum, *J. Geophys. Res.* **72**, no. 4, 1217–1231.
- Bird, P. (2003). An updated digital model of plate boundaries, *Geochem. Geophys. Geosys.* **4**, no. 3, doi: [10.1029/2001GC000252](https://doi.org/10.1029/2001GC000252).
- Boatwright, J. (1980). A spectral theory for circular seismic sources; simple estimates of source dimension, dynamic stress drop, and radiated seismic energy, *Bull. Seismol. Soc. Am.* **70**, no. 1, 1–27.
- Boatwright, J. (2007). The persistence of directivity in small earthquakes, *Bull. Seismol. Soc. Am.* **97**, no. 6, 1850–1861.
- Brune, J. N. (1970). Tectonic stress and the spectra of seismic shear waves from earthquakes, *J. Geophys. Res.* **75**, no. 26, 4997–5009.
- Brune, J. N. (1971). Seismic sources, fault plane studies and tectonics, *Eos Trans. AGU* **52**, no. 5, IUGG-178–IUGG-187.
- Chai, G., S. H. Yoo, J. Rhie, and T. S. Kang (2020). Stress-drop scaling of the 2016 Gyeongju and 2017 Pohang earthquake sequences

- using coda-based methods, *Bull. Seismol. Soc. Am.* **110**, no. 5, 2047–2057.
- Chang, K. H., and X. Zhao (2012). North and South China suturing in the east end: What happened in Korean Peninsula? *Gondwana Res.* **22**, no. 2, 493–506.
- Choi, S., I.-C. Ryu, and H.-J. Götze (2015). Depth distribution of the sedimentary basin and Moho undulation in the Yellow Sea, NE Asia interpreted by using satellite-derived gravity field, *Geophys. J. Int.* **202**, 41–53.
- Chough, S. K., H. Kim, J. Woo, and H. S. Lee (2006). Tectonic implications of quartzite-shale and phyllite beds in the Seochangri Formation (Okcheon group), Bonghwajae section, mid-Korea, *Geosci. J.* **10**, 403–421.
- Chough, S. K., S. T. Kwon, J. H. Ree, and D. K. Choi (2000). Tectonic and sedimentary evolution of the Korean peninsula: A review and new view, *Earth Sci. Rev.* **52**, no. 1/3, 175–235.
- Deichmann, N., and M. Garcia-Fernandez (1992). Rupture geometry from high-precision relative hypocentre locations of microearthquake clusters, *Geophys. J. Int.* **110**, no. 3, 501–517.
- Eshelby, J. D. (1957). The determination of the elastic field of an ellipsoidal inclusion, and related problems, *Proc. Roy. Soc. Lond. A* **241**, no. 1226, 376–396.
- Han, S., W. Y. Kim, H. Lim, Y. O. Son, M. S. Seo, J. Y. Park, and Y. Kim (2024). Resolving multi-stage rupture process of the 2021  $M_w$  4.9 Offshore Jeju Island earthquake from relative source time functions, *Geophys. Res. Lett.* **51**, no. 3, e2023GL106059, doi: [10.1029/2023GL106059](https://doi.org/10.1029/2023GL106059).
- Harris, D. B. (1991). A waveform correlation method for identifying quarry explosions, *Bull. Seismol. Soc. Am.* **81**, no. 6, 2395–2418.
- Hong, T. K., and H. Choi (2012). Seismological constraints on the collision belt between the North and South China blocks in the Yellow Sea, *Tectonophysics* **570**, 102–113.
- Hu, P., X. Yang, F. Yang, J. Zhang, Z. Zhou, and R. Dong (2022). Seismogenic structure and tectonic mechanism of the 2021  $M_w$  5.0 Yancheng earthquake in the South Yellow Sea basin, East Asia, *Seismol. Res. Lett.* **94**, 646–670.
- Kane, D. L., P. M. Shearer, B. P. Goertz-Allmann, and F. L. Vernon (2013). Rupture directivity of small earthquakes at Parkfield, *J. Geophys. Res.* **118**, no. 1, 212–221.
- Kaneko, Y., and P. M. Shearer (2014). Seismic source spectra and estimated stress drop derived from cohesive-zone models of circular subshear rupture, *Geophys. J. Int.* **197**, no. 2, 1002–1015.
- Kato, N. (2009). A possible explanation for difference in stress drop between intraplate and interplate earthquakes, *Geophys. Res. Lett.* **36**, no. 23, doi: [10.1029/2009GL040985](https://doi.org/10.1029/2009GL040985).
- Kennett, B.L.N. (1986). *Lg* waves and structural boundaries, *Bull. Seismol. Soc. Am.* **76**, 1133–1141.
- Kennett, B. L. N., and E. R. Engdahl (1991). Travel times for global earthquake location and phase identification, *Geophys. J. Int.* **105**, no. 2, 429–465.
- Kennett, B. L. N., E. R. Engdahl, and R. Buland (1995). Constraints on seismic velocities in the Earth from travel times, *Geophys. J. Int.* **122**, no. 1, 108–124.
- Kim, S. J., and S. G. Kim (1983). A study on the crustal structure of South Korea by using seismic waves, *Econ. Environ. Geol.* **16**, no. 1, 51–61.
- Kim, W. Y. (1987). Modelling short-period crustal phases at regional distances for the seismic source parameter inversion, *Phys. Earth Planet. In.* **47**, 159–178.
- Kim, W. Y., and K. H. Kim (2014). The 9 February 2010 Siheung, Korea, earthquake sequence: Repeating earthquakes in a stable continental region, *Bull. Seismol. Soc. Am.* **104**, no. 1, 551–559.
- Kim, W. Y., H. Choi, and M. Noh (2010). The 20 January 2007 Odaesan, Korea, earthquake sequence: Reactivation of a buried strike-slip fault? *Bull. Seismol. Soc. Am.* **100**, no. 3, 1120–1137.
- Kim, W.-Y., N. Noh, and H. Choi (2006). The 29 May 2004 offshore southeast coast of Korea earthquake sequence: Shallow earthquakes in the Ulleung back-arc basin, East Sea (Sea of Japan), *J. Korean Geophys. Soc.* **9**, 249–262.
- Kim, W.-Y., J. Y. Park, M. S. Seo, Y. O. Son, H. Lim, S. Han, and Y. Kim (2022). The 14 December 2021  $M_w$  4.9 offshore Jeju Island, Korea, earthquake: Seismological observation of an intraplate earthquake provides insight into regional seismotectonics, *Seism. Rec.* **2**, no. 2, 107–117.
- Kim, W.-Y., M. S. Seo, J. Y. Park, S. Han, Y. O. Son, and Y. Kim (2023). The 28 October 2022  $M_w$  3.8 Goesan earthquake sequence in central Korea: Stress drop, aftershock triggering, and fault interaction, *Bull. Seismol. Soc. Am.* **113**, no. 6, 2416–2431.
- Klein, F. W. (2002). User's guide to HYPOINVERSE-2000, a Fortran program to solve for earthquake locations and magnitudes, *U.S. Geol. Surv. Open-File Rept.* **02-171**.
- Knopoff, L., F. Schwab, and E. Kausel (1973). Interpretation of *Lg*, *Geophys. J. Int.* **33**, no. 4, 389–404.
- Morris, A., D. A. Ferrill, and D. B. Henderson (1996). Slip-tendency analysis and fault reactivation, *Geology* **24**, no. 3, 275–278.
- Oh, C. W. (2006). A new concept on tectonic correlation between Korea, China and Japan: Histories from the late Proterozoic to Cretaceous, *Gondwana Res.* **9**, nos. 1/2, 47–61.
- Onwuemeke, J., Y. Liu, and R. M. Harrington (2018). Earthquake stress drop in the Charlevoix seismic zone, eastern Canada, *Geophys. Res. Lett.* **45**, no. 22, 12–226.
- Paige, C. C., and M. A. Saunders (1982). Algorithm 583: LSQR: Sparse linear equations and least squares problems, *ACM Trans. Math. Software* **8**, no. 2, 195–209.
- Park, J.-C., W. Kim, T. W. Chung, C.-E. Baag, and J.-H. Ree (2007). Focal mechanisms of recent earthquakes in the southern Korean peninsula, *Geophys. J. Int.* **169**, 1103–1114.
- Park, S. C., M. K. Kong, E. H. Park, W. Y. Yun, and I. K. Hahm (2012). Source parameters of the 2011 Yellow Sea earthquake ( $M_L$  5.3): Different features from earthquakes on the Korean peninsula, *Earth Planets Space* **64**, no. 5, 379–388.
- Prieto, G. A., R. L. Parker, and F. L. Vernon III (2009). A Fortran 90 library for multitaper spectrum analysis, *Comput. Geosci.* **35**, no. 8, 1701–1710.
- Rhie, J., and S. Kim (2010). Regional moment tensor determination in the southern Korean peninsula, *Geosci. J.* **14**, 329–333.
- Schaff, D. P., and P. G. Richards (2004a). Repeating seismic events in China, *Science* **303**, no. 5661, 1176–1178.
- Schaff, D. P., and P. G. Richards (2004b). *Lg*-wave cross correlation and double-difference location: Application to the 1999 Xiuyan, China, sequence, *Bull. Seismol. Soc. Am.* **94**, no. 3, 867–879.
- Schaff, D. P., W. Y. Kim, P. G. Richards, E. Jo, and Y. Ryoo (2018). Using waveform cross correlation for detection, location, and

- identification of aftershocks of the 2017 nuclear explosion at the North Korea test site, *Seismol. Res. Lett.* **89**, no. 6, 2113–2119.
- Schaff, D. P., P. G. Richards, M. Slinkard, S. Heck, and C. Young (2018). Lg-wave cross correlation and epicentral double-difference location in and near China, *Bull. Seismol. Soc. Am.* **108**, no. 3A, 1326–1345.
- Scholz, C. H., C. A. Aviles, and S. G. Wesnousky (1986). Scaling differences between large interplate and intraplate earthquakes, *Bull. Seismol. Soc. Am.* **76**, no. 1, 65–70.
- Seekins, L. C., and J. Boatwright (2010). Rupture directivity of moderate earthquakes in northern California, *Bull. Seismol. Soc. Am.* **100**, no. 3, 1107–1119.
- Shi, J., W. Y. Kim, and P. G. Richards (1996). Variability of crustal attenuation in the northeastern United States from Lg waves, *J. Geophys. Res.* **101**, no. B11, 25,231–25,242.
- Slinkard, M., S. Heck, D. Schaff, N. Bonal, D. Daily, C. Young, and P. Richards (2016). Detection of the Wenchuan aftershock sequence using waveform correlation with a composite regional network, *Bull. Seismol. Soc. Am.* **106**, no. 4, 1371–1379.
- Soh, I., C. Chang, J. Lee, T. K. Hong, and E. S. Park (2018). Tectonic stress orientations and magnitudes, and friction of faults, deduced from earthquake focal mechanism inversions over the Korean peninsula, *Geophys. J. Int.* **213**, no. 2, 1360–1373.
- Son, M., J. S. Shin, G. Kim, and C. S. Cho (2015). Epicenter relocation of two 2013 earthquake sequences in the Yellow Sea, Korea, using travel-time double-differences and Lg-wave cross-correlation, *Geosci. J.* **19**, no. 2, 295–303.
- Son, Y. O., M. S. Seo, and Y. Kim (2022). Measurement of seismometer misorientation based on P-wave polarization: Application to permanent seismic network in South Korea, *Geosci. J.* **26**, no. 2, 235–247.
- Tenthorey, E., and S. F. Cox (2006). Cohesive strengthening of fault zones during the interseismic period: An experimental study, *J. Geophys. Res.* **111**, no. B9, doi: [10.1029/2005JB004122](https://doi.org/10.1029/2005JB004122).
- Uchide, T., and K. Imanishi (2016). Small earthquakes deviate from the omega-square model as revealed by multiple spectral ratio analysis, *Bull. Seismol. Soc. Am.* **106**, no. 3, 1357–1363.
- Uchide, T., and S. G. Song (2018). Fault rupture model of the 2016 Gyeongju, South Korea, earthquake and its implication for the underground fault system, *Geophys. Res. Lett.* **45**, no. 5, 2257–2264.
- Uchide, T., T. Shiina, and K. Imanishi (2022). Stress map of Japan: Detailed nationwide crustal stress field inferred from focal mechanism solutions of numerous microearthquakes, *J. Geophys. Res.* **127**, no. 6, e2022JB024036, doi: [10.1029/2022JB024036](https://doi.org/10.1029/2022JB024036).
- Viegas, G., R. E. Abercrombie, and W. Y. Kim (2010). The 2002 M 5 Au Sable Forks, NY, earthquake sequence: Source scaling relationships and energy budget, *J. Geophys. Res.* **115**, no. B7, doi: [10.1029/2009JB006799](https://doi.org/10.1029/2009JB006799).
- Waldhauser, F. (2001). hypoDD—A program to compute double-difference hypocenter locations, *U.S. Geol. Surv. Open-File Rept.* **2001-113**.
- Waldhauser, F., and W. L. Ellsworth (2000). A double-difference earthquake location algorithm: Method and application to the northern Hayward fault, California, *Bull. Seismol. Soc. Am.* **90**, no. 6, 1353–1368.
- Wu, Q., and M. Chapman (2017). Stress-drop estimates and source scaling of the 2011 Mineral, Virginia, mainshock and aftershocks, *Bull. Seismol. Soc. Am.* **107**, no. 6, 2703–2720.
- Yin, A., and S. Nie (1993). An indentation model for the North and South China collision and the development of the Tan-Lu and Honam fault systems, eastern Asia, *Tectonics*, **12**, no. 4, 801–813.
- Yoon, C. E., N. Yoshimitsu, W. L. Ellsworth, and G. C. Beroza (2019). Foreshocks and mainshock nucleation of the 1999  $M_w$  7.1 Hector Mine, California, earthquake, *J. Geophys. Res.* **124**, no. 2, 1569–1582.
- Yoshimitsu, N., W. L. Ellsworth, and G. C. Beroza (2019). Robust stress drop estimates of potentially induced earthquakes in Oklahoma: Evaluation of empirical Green's function, *J. Geophys. Res.* **124**, no. 6, 5854–5866.
- Zhao, L. S., and D. V. Helmberger (1994). Source estimation from broadband regional seismograms, *Bull. Seismol. Soc. Am.* **84**, 91–104.
- Zheng, X.-F., Z.-X. Yao, J.-H. Liang, and J. Zheng (2010). The role played and opportunities provided by IGP DMC of China National Seismic Network in Wenchuan earthquake disaster relief and researches, *Bull. Seismol. Soc. Am.* **100**, no. 5B, 2866–2872.

---

Manuscript received 23 April 2024

Published online 8 October 2024